Research Square

Preprints are preliminary reports that have not undergone peer review.
They should not be considered conclusive, used to inform clinical practice,
or referenced by the media as validated information.

High performance core-shell Fe_2O_3@N-C anode materials derived from iron concentrate leachate for lithium-ion batteries

Yihao Peng
Kunming University of Science and Technology
Yu Song
Kunming University of Science and Technology
Li Wang
Hebei Normal University for Nationalities Chengde
Yunke Wang
Yunnan open university
Yin Li
510527335@qq.com

Kunming University of Science and Technology
Yaochun Yao
Kunming University of Science and Technology

Research Article

Keywords: Lithium-ion battery, Anode material, Fe2O3@N-C composite, Iron concentrate leachate

Posted Date: June 3rd, 2026

DOI: https://doi.org/10.21203/rs.3.rs-9409336/v1

License: This work is licensed under a Creative Commons Attribution 4.0 International License.
Read Full License

Additional Declarations: No competing interests reported.

Abstract

Fe_2O_3, as a lithium-ion battery (LIB) anode material, features high specific capacity, resource abundance, cost-effectiveness and eco-friendliness, but suffers from large volume changes, poor cycling performance, and significant first-cycle irreversible capacity loss. Here, we demonstrate that these challenges can be tackled by using a fully exploited N-doped carbon (Fe_2O_3@N-C) via ZIF-67. An indepth analysis demonstrates that N-doped carbon alleviates the volume expansion and enhances ionic conductivity. This enhancement arises from a cavity was generated between the Fe_2O_3 and carbon layer during the carbonization process and nitrogen-doped carbon layers are formed. As a result, the Fe_2O_3@N-C composite exhibits exceptional cycling and rate performance. At a current density of 1 A g^{-1}, it maintains a discharge capacity of 782.9 mAh g^{-1} after 300 cycles with a charge/discharge efficiency of 99.4%, significantly surpassing the 205.37 mAh g^{-1} achieved by pure Fe_2O_3. Even at 5 A g^{-1}, Fe_2O_3@N-C delivers a discharge capacity of 202.39 mAh g^{-1}, while Fe_2O_3 only achieves 4.72 mAh g^{-1}. This study provides a novel strategy for utilizing iron concentrate and transition metal oxides in high-performance LIB anodes.

1.Introduction

Lithium-ion batteries (LIBs) are widely used in portable electronics, electric vehicles, and grid-scale energy storage systems due to their high operating voltage, high energy density, and long cycle life. A typical LIB consists of a cathode, an anode, a separator, and an electrolyte[1]. As a critical component, the anode material governs key performance metrics, including lithium-ion intercalation/deintercalation kinetics, reversible capacity, solid-electrolyte interphase (SEI) formation, cycle life, and safety[2]. Even though the standard commercial graphite anode material has achieved its theoretical capacity of 372 mAh g^{-1}, it continues to fall short of the requirements for massive energy storage infrastructures[3, 4]. Consequently, an urgent requirement exists for new anode materials for lithium-ion batteries that offer better energy density and cycling stability. Over the past decades, due to their unique characteristics and potential applications, transition metal oxides have garnered considerable attention from scientists[5]. These include iron oxide (Fe_2O_3), on account of its significant theoretical capacity (1007 mAh g^{-1}), sustainability, and economical nature, is among the most promising options for anode materials in lithium-ion batteries[6, 7]. However, while charging and discharging, Fe_2O_3 suffers from low conductivity and significant volume expansion, resulting in severe capacity fading and irreversible electrode polarization during cycling[8]. To address these issues, a lot of work has been done to enhance the structural integrity and cycling stability of Fe_2O_3 anode materials. The primary approach involves creating nanostructures or applying a coating of conductive carbon materials like amorphous carbon, graphene, and carbon nanotubes[9]. Building nanostructures can reduce volumetric effects during charging and discharging, while also increasing electroactive sites and decreasing diffusion distances for lithium ions and electrons[10]. A range of Fe_2O_3 composite materials with nanostructures, such as nanoparticles[11], nanorods[12], nanotubes[13], nanosheets[14], and 3D hierarchical nanostructures[15], have been documented and have shown enhanced lithium storage capabilities. Combining with carbon-

based materials significantly improves the electronic conductivity and structural integrity of electroactive materials, increasing the cycling stability and performance at high rates of electrodes[16–18]. However, these strategies often involve complex synthesis or expensive precursors, limiting scalability. Metal-organic frameworks (MOFs) like ZIF-67 offer a solution by enabling in-situ growth of conductive, porous carbon matrices.

Metal-organic frameworks (MOFs) are structures created by the self-assembly of metal ions or clusters connected to organic ligands through coordination bonds. MOFs, as promising substances featuring high porosity and a significant specific surface area[19], have been applied in fields such as catalysis[20], gas separation[21], sensors[22], and energy storage[23]. Lately, MOFs have been utilized as a simple and efficient method for preparing porous derivatives (including metals[24], metal sulfides[25], metal oxides[26], as well as their carbon-based composites[27]). The morphology and porous structure of MOF precursors are typically inherited by metal-based derivatives, increasing their conductivity and stability for electrochemical purposes[28]. Moreover, when employed as anode components for lithium-ion batteries, MOF-derived porous materials not only offer an elevated specific surface area and porosity to increase contact involving electrolytes and nanomaterials but also provide more active sites and shorter diffusion paths to accelerate lithium-ion diffusion.

Iron concentrate, as one of the higher-quality and higher-iron-content types of iron ore. It is frequently applied in steel, metallurgy, industries related to chemicals, and other fields, with high market demand, leading to a gradual expansion of the iron concentrate industry market size. Nevertheless, due to limited domestic iron ore reserves and heavy reliance on imports, so the economic and efficient recovery of valuable metals from iron concentrate has become a pressing priority. Considering the low cost of iron concentrate and the material advantages of Fe_2O_3 electrodes.

Therefore, in this study, we used iron concentrate leachate as the iron source to prepare Fe_2O_3 applied as lithium-ion battery anode. The price comparison between other iron sources for preparing Fe_2O_3 and iron concentrate is evident in Table 1. To enhance the electrochemical efficiency of Fe_2O_3, we in-situ grew ZIF-67 on the surface of Fe_2O_3 and successfully synthesized the hollow framework structure of Fe_2O_3@N-C composite material through carbonization. The hollow framework design can efficiently prevent the volume expansion of Fe_2O_3 during charging and discharging. The prepared Fe_2O_3@N-C material demonstrated excellent electrochemical efficiency when serving as lithium-ion battery anode. When the current density was maintained at 1 A g^{-1}, the Fe_2O_3@N-C electrode exhibited a discharge capacity of 782.9 mAh g^{-1} after 300 cycles, with a Coulombic efficiency of 99.4%, far exceeding the 205.37 mAh g^{-1} of pure Fe_2O_3. By conducting rate performance tests on Fe_2O_3 and Fe_2O_3@N-C, at a current density of 5 A g^{-1}, the corresponding discharge capacities were measured at 4.72 mAh g^{-1} and 202.39 mAh g^{-1}, respectively, indicating the outstanding electrochemical capabilities of Fe_2O_3@N-C even at high current densities.

Table 1
Comparison of iron concentrate with other iron sources for Fe_2O_3 preparation.

Iron Source(dollar/ton)	Iron Concentrate (This Study)	Ferrous Oxalate	Ferrous Sulfate	Ferrous Chloride	Ferric Nitrate
Current Price (as of 2025-01-12)	98.6	1432.5	395.49	1,636.53	436.41

2. Experimental section

2.1. Raw materials

The iron concentrate for this research was obtained from a company situated in Yunnan, China. Ammonia ($NH_3{\cdot}H_2O$), analytically pure, from China National Pharmaceutical Group Chemical Reagent Co., Ltd. $Co(NO_3)_2{\cdot}6H_2O$, analytically pure, from the same source; polyvinylpyrrolidone (PVP), analytically pure, and 2-methylimidazole, analytically pure, also from the same supplier.

2.2. Preparation of Fe_2O_3 and Fe_2O_3@N-C

Using iron concentrate leachate as the iron source (The optimal leaching conditions were determined to be a liquid-to-solid ratio of 15:1, duration of 4 h, temperature of 90°C, and sulfuric acid concentration of 40%; The variation in ion concentrations before and after leaching is presented in Table S1.) and ammonia as the precipitant, ferric hydroxide was prepared at room temperature through a simple chemical precipitation method. It was then washed, dried, and calcined at 500 ℃ for 2 h in a vacuum tube furnace to yield ferric oxide. A mixture of 0.5 g of ferric oxide and 0.5 g of PVP was stirred in 100 mL methanol solution for 30 minutes. Then, 0.6527 g $Co(NO_3)_2{\cdot}6H_2O$ was added and ultrasonicated for 30 min to prepare solution A (Fe_2O_3:ZIF-67 = 2:1). Dissolved 1.472 g of 2-methylimidazole into 50 mL methanol solution to prepare solution B (Co:Hmeim = 1:4). Using a burette, solution B was gradually introduced to solution A while stirring at 400 rpm. Once fully added, the mixture was stirred continuously for 24 hours. The product was subjected to five rinsing cycles using methanol and deionized water, then dried in a vacuum oven at 80 ℃ for 12 hours. And then the sample was then maintained at 500°C for 2 hours in a vacuum drying oven under an argon-hydrogen gas mixture (heating rate: 5°C/min) to obtain the Fe_2O_3@N-C composite material. The synthetic process of Fe_2O_3@N-C as shown in Scheme 1.

2.3. Material characterization

XRD (Austrian Anton Paar XRDynamic500) was used to examine the crystal structure of the synthesized material. The morphology of the samples was examined using SEM (German ZEISS Fegma 300) and TEM (US FEI Talos F200x). X-ray photoelectron spectroscopy (XPS) was conducted using a Thermo Scientific K-Alpha analyzer to analyze the surface chemical composition and valence states. Nitrogen adsorption-desorption isotherms were measured using a US Micromeritics ASAP 2460 analyzer to determine the specific surface area of the samples.

2.4. Electrochemical measurements

The anode was prepared using a slurry coating method. Fe_2O_3 or Fe_2O_3@N-C, PVDF, and Super P were mixed in a 7:2:1 mass ratio and dissolved in N-methyl-2-pyrrolidone (NMP) to form a uniform slurry. Subsequently, the slurry was applied to copper foil and vacuum-dried at 80°C for 12 h. Additionally, the electrodes were cut into 14 mm diameter disks with an active material loading of 39.11 ± 0.05 mg/cm^2. The liquid electrolyte consisted of 1 M $LiPF_6$ dissolved in a 1:1:1 volumetric mixture of ethylene carbonate (EC), dimethyl carbonate (DMC), and ethyl methyl carbonate (EMC). CR2025 coin cells were assembled within an argon-filled glovebox. A battery testing system (BTS 3000, Neware, China) was employed to conduct constant-current charge-discharge tests at 25°C within a voltage range of 0.01-3 V (vs. Li^+/Li) under varying current densities. Cyclic voltammetry (CV) analyses were performed using an electrochemical workstation (Chi 760 E, China) within a potential range of 0.01-3 V (vs. Li^+/Li) at scan rates of 0.1-1 mV s^{-1}. Electrochemical impedance spectroscopy (EIS) measurements were performed across a frequency range of 10 mHz to 100 kHz.

3. Result and discussion

Figure 1a presents the X-ray diffraction (XRD) spectra of pure Fe_2O_3 and the composite Fe_2O_3@N-C. The diffraction peaks of the samples align consistently with the rhombohedral phase of Fe_2O_3(PDF#33–0664), confirming that selective precipitation prevents the trace impurities in the iron concentrate from affecting the crystal phase structure of Fe_2O_3[29]. Additionally, the diffraction peaks after coating Fe_2O_3 with ZIF-67 nanoparticles and carbonization align with those in PDF#75 – 0033. Fe_2O_3 and Fe_2O_3@N-C exhibit different PDF cards primarily due to during the carbon-coating process, the α-Fe_2O_3 precursor was partially reduced to γ-Fe_2O_3 by the ZIF-67-derived carbon matrix. XRD analysis (PDF#75 – 0033) confirmed the dominant γ-phase formation, which aligns with previous reports demonstrating no adverse effects on electrochemical performance[30]. The diffraction peak intensity of Fe_2O_3 is notably reduced after coating. This is because ZIF-67 forms an amorphous structure during the coating process, which does not produce distinct diffraction peaks but overlaps with those of Fe_2O_3, thus reducing the intensity of the diffraction peaks of Fe_2O_3[31].

Figures 1(b-e) shows SEM images of Fe_2O_3 and Fe_2O_3@N-C at magnifications of 500 nm and 100 nm. Figures 1(d,e) depict SEM images of Fe_2O_3, exhibits the synthesized Fe_2O_3 features a structure, irregular nanoparticles, with pronounced particle stacking. Compared to the SEM images of Fe_2O_3, it is evident that after the coating process, the boundaries between particles are distinct, and individual particle structures are more intact, as shown in Figs. 1(b,c). This provides the sample having a greater surface area, exposing extra active sites and help to reduce the reaction energy barrier. Additionally, nanoscale particle growth is observed on the surface of Fe_2O_3, indicating successful coating with ZIF-67. After coating, the particle size becomes more uniform. Such a structure significantly strengthens the stability of electrode materials during electrochemical cycling[32].

Figures 2 (a-c) present TEM images of Fe_2O_3 at different magnifications, showing that the surfaces of the Fe_2O_3 particles are relatively smooth. Figures 2d-f are TEM images of Fe_2O_3@N-C. After the coating process, the Fe_2O_3 surface is coated with ZIF-67. As shown in Fig. 2f, the Fe_2O_3 particle surface is clearly encased in a layer of graphite carbon, thereby improving the ability of the material to conduct electricity. Fe_2O_3 is embedded within a carbon matrix derived from ZIF-67, which provides spaces to buffer the volume changes of Fe_2O_3 during charge and discharge. Figures 2(g-l) display the elemental mapping images of the samples. The findings show that the composite has a uniform distribution of mixed elements, with C in blue, N in cyan, O in red, Fe in green, and Co in orange, with Fe_2O_3 located at the core of the composite. The successful incorporation of N will effectively enhances the conductivity and promotes lithium-ion transport of material. This verifies that Fe_2O_3 particles are surrounded by a carbon layer and incorporated into the NC-ZIF matrix, aligning with the SEM and TEM findings.

The core-shell structure of the synthesized samples was examined using N_2 adsorption and desorption isotherm analysis. As illustrated in Fig. 3a, the Fe_2O_3@N-C demonstrates a type IV isotherm featuring a hysteresis loop within the P/P0 range of 0.75 to 1.0, showing that there is a large number of mesopores. Minimal N_2 adsorption at P/P0 < 0.1 suggests that the number of micropores is extremely limited. Isotherms were used to calculate the pore size profile of the sample. Figure 3b demonstrates that the pore size is predominantly distributed ranging from 0 to 50 nm, indicating the structure has a hierarchy of pores, including both micropores and mesopores in Fe_2O_3@N-C, favoring electrolyte infiltration and ion transport. The presence of abundant pores contributes to forming an interlocking structure, which improves resistance to volume variations during the lithiation and delithiation process. Using the BET and BJH methods, the specific surface area was determined to be 31.83 m^2 g^{-1}, with an average pore width of 13.65 nm.

The chemical valence states and elemental makeup of the Fe_2O_3@N-C composite were examined using XPS (X-ray photoelectron spectroscopy). Figure 4a displays the entire spectrum, indicating that Fe_2O_3@N-C includes the elements C, Co, N, O, and Fe. According to Fig. 4b, the spectral analysis of Co 2p is mainly characterized by peaks at 780.35, 782.87, 786.09, 788.86, 796.17, and 802.87 eV. Primarily, the peaks at 780.35 and 788.86 eV are satellite peaks of Co 2p, and the peaks at 782.87 and 796.17 eV relate to Co^{2+} and those at 786.09 and 802.87 eV are mainly attributed to Co^{3+}, indicating partial surface oxidation of the Fe_2O_3@N-C composite [33]. The peaks at 710.09 and 724.60 eV in the Fe 2p XPS spectrum correspond to Fe $2p_{3/2}$ and Fe $2p_{1/2}$, respectively (Fig. 4c). The peaks at 718.75 and 732.60 to satellite peaks of Fe 2p [34]. The O 1s XPS spectrum displays peaks at 529.52 eV and 531.32 eV, corresponding to Fe-O-Fe and Fe-O-C, respectively (Fig. 4d). Four peaks are observed in the N 1s spectrum, located at 399.05, 400.14, 401.27 and 401.94 eV (Fig. 4e), corresponding to graphitic nitrogen, pyrrolic nitrogen, pyridinic nitrogen and oxidized nitrogen, respectively. The successful doping of N into the C layer is indicated, leading to improved conductivity of the material [35]. Figure 4f, the peaks at 284.4, 286.1, and 288.45 eV in the C 1s XPS spectrum are linked to C-C, C-O, and O-C = O bonds, respectively[36]. To further investigate the cycling stability, XPS analysis was conducted on Fe_2O_3@N-C

electrodes after 100 cycles at 1A g^{-1} (Fig. S2). The post-cycling XPS spectra exhibit nearly identical characteristic features compared to the pristine material, indicating excellent chemical stability of Fe_2O_3@N-C during electrochemical cycling[37].

Figures 5a and b show the CV curves for Fe_2O_3 and Fe_2O_3@N-C using a scan speed of 0.1 mV/s. The initial CV cycle shows that both electrodes have comparable characteristics (Fig. 5a). During the initial cathodic scan, a significant reduction peak around 0.65 V is noted, linked to the conversion of Fe^{3+}/Fe^{2+} to Fe^0 and the creation of the solid electrolyte interface (SEI) film[38]. During the reverse anodic scan, a wide oxidation peak around 1.65 V is detected, indicating the oxidation of Fe^0 to Fe^{2+} and Fe^{2+} to Fe^{3+} [39]. In later cycles, as the cycle count rises, the oxidation and strong reduction peaks for both electrode materials move to higher voltages, accompanied by a notable decrease in peak height. The movement of reduction and oxidation peaks to higher voltages is probably caused by irreversible structural changes and SEI formation during the initial discharge/charge cycles[40]. Additionally, with an increasing number of cycles, the area of the redox peaks in the CV curves diminishes, indicating capacity fading during the discharge/charge cycles.

Figure 5c demonstrates the long-cycle performance of Fe_2O_3 and Fe_2O_3@N-C at 1 A g^{-1}. Following 300 cycles, the discharge capacities of Fe_2O_3@N-C and Fe_2O_3 are 782.9 mAh g^{-1} and 205.37 mAh g^{-1}, respectively. Figure 5d presents the rate performance of Fe_2O_3 and Fe_2O_3@N-C under varying current densities, demonstrating that the rate efficiency of Fe_2O_3@N-C is superior to Fe_2O_3 after coating. Despite with a current density reaching 5 A g^{-1}, Fe_2O_3@N-C retains a discharge specific capacity of 202.39 mAh g^{-1}, while Fe_2O_3 achieves only 4.72 mAh g^{-1}. Figures 5e and f represent the charge and discharge profiles of Fe_2O_3 and Fe_2O_3@N-C across various cycles. The first discharge curves for both electrodes feature a lengthy plateau around 0.86 V, followed by a downward slope at 0.01 V. The primary charging curve shows an inclined plateau between 1.5 and 2.0 V. As the cycle number increases the discharge and charge plateaus gradually become shorter from 1 to 50, causing a drop in capacity. Between 100 and 300 cycles, the discharge and charge plateaus extend, leading to a rise in reversible capacity. From Fig. 5e, the discharge specific capacity of Fe_2O_3 exhibits an initial decline followed by stabilization between 1–300 cycles, showing a capacity loss of 568.05 mAh g^{-1} from cycles 1–50 and an initial coulombic efficiency of only 62.79%. This increasing capacity upon cycling can be due to the refinement of electroactive materials, which could increase the electroactive area of active materials, offer additional interfacial charge storage, and induce the unconventional activity of structural defects[40]. Figure 5f shows the charge-discharge curves of Fe_2O_3@N-C across different cycles, where the discharge capacity first decreases and then increases. Between cycles 1–50, the capacity fades by 450.94 mAh g^{-1}, starting with a coulombic efficiency of 66.52%. The electrochemical performance comparison with previously reported Fe_2O_3 materials is presented in Table 2.

The marked improvement in electrochemical performance is due to the following reasons: (1) The ZIF-67 organic framework structure synthesized on the surface of Fe_2O_3 can mitigate the expansion and

contraction of volume of electrode materials as the charge and discharge occur, decreasing discharge capacity reduction and boosting the cycling and rate performance of Fe_2O_3. (2) The successful doping of N derived from the ZIF-67 framework enhances the ionic conductivity of Fe_2O_3 materials, promotes ion transport, and increases discharge capacity.

Table 2
Electrochemical performance comparison with references.

Sample	**Capacity (mAh g^{-1})**	**Ref**
Fe_2O_3/MOFs	782.4 at 0.5 A g^{-1}	[8]
Hollow Fe_2O_3 Nanorods	767 at 0.5 A g^{-1}	[10]
Porous Fe_2O_3 nanotubes	613.7 at 0.5 A g^{-1}	[13]
Fe_2O_3@N-C	782.9 at 0.5 A g^{-1} 202.39 at 5 A g^{-1}	This work

In order to examine the electrochemical behavior of Fe_2O_3@N-C further, CV curves of Fe_2O_3@N-C electrodes were measured at various scan rates. As the scan rate is raised from 0.2 to 1 mV s^{-1}, there was a significant increase in the anodic and cathodic peak currents, suggesting fast reaction kinetics and highly reversible lithium storage (Fig. 6a). The correlation between peak current (I) and scan rate (v) in CV curves[41]:

$i = av^{\square}$ (1)

The logarithmic relationship between peak current and scan rate can be used to analyze electrochemical kinetic. When b equals 0.5, it points to diffusion-controlled capacity, while b value of 1.0 signifies that pseudocapacitance is the main factor in electrochemical reactions. Fig. 6b illustrates that the linear correlation between the logarithm of peak current and scan rate from 0.2 to 1 mV s^{-1} results in a b-value of 0.75. This finding suggests that the Fe_2O_3@N-C electrode operates through both pseudocapacitance and diffusion mechanisms, unlike traditional Fe-based anodes that are only diffusion-controlled. The cumulative stored charge capacitive contribution is capable of being measured using these equations[42] :

$i(V) = k_1v + k_2v^{1/2}$ (2)

$i(V)/v^{1/2} = k_1v^{1/2} + k_2$ (3)

In the context of cyclic voltammetry (CV), the current output at a certain voltage is denoted by i(V), with k_1v and $k_2v^{1/2}$ representing the capacitive and diffusion-controlled currents. Eq. (3) can be used to fit the

CV data and determine values for k_1 and k_2.

When scanning at 1 mV s^{-1}, pseudocapacitance contributes 83.63% to the storage of Li^+(Fig. 6c). Figure 6d displays the contributions of charges controlled by pseudocapacitance and diffusion at diverse scan rates. With an increase in the scan rate, the charge transfer rate also rises, leading to a higher proportion of pseudocapacitance contribution. An analysis was performed to examine the dominant role of pseudocapacitive behavior in the storage and release of Li^+ at elevated scan rates, alongside the rapid charge-discharge characteristics of the capacitive storage framework. A deeper mechanistic analysis reveals that the pseudocapacitance arises primarily from the unique carbon framework, which offers numerous active sites and N-doping defects, leading to extra Li storage.

To further investigate the Li^+ storage properties of Fe_2O_3@N-C composites, electrochemical impedance spectroscopy was executed at 25 °C, spanning frequencies from 0.01 Hz to 100 kHz (Fig. 7a). In the Nyquist plot, a depressed semicircle appears in the medium and high-frequency areas, while a diagonal line is present in the low-frequency area. The SEI layer resistance (R_e) and charge transfer resistance (R_1) at the electrode-electrolyte interface are responsible for the medium and high-frequency regions. In the solid electrode material, the diagonal line signifies the Warburg diffusion resistance (Z_w), concerning the diffusion of Li^+ ions in the solid-state active component [43, 44]. Through the process of curve fitting, the initial R_1 values for Fe_2O_3 and Fe_2O_3@N-C composites were determined to be 126.8 Ω and 57.02 Ω, respectively. The introduction of the carbon layer significantly enhanced the charge transfer rate of the Fe_2O_3@N-C composite. According to previous reports, the lithium-ion diffusion rate can be calculated using Equations (4) and (5) in Fig. 7b:

$$Z = Rs + Rf + \sigma_w \omega^{-0.5} \quad (4)$$

$$D_{Li} = R^2T^2 / 2A^2n^4F^4C^2\sigma^2_w \quad (5)$$

Where, in the low-frequency region, ω represents the angular frequency, T represents the temperature in Kelvin, which is 298 K, and R stands for the gas constant, valued at 8.314 J $mol^{-1}K^{-1}$, A represents the area where work is effectively performed (cm^2), n stands for the moles of electrons participating in the redox reaction, C signifies the concentration of lithium ions (mol/L), F is the Faraday constant (C mol^{-1}), and σ_w is the Warburg coefficient associated with Z´. Table 3 summarizes the EIS fitting parameters, Warburg factors, and ionic conductivity values for Fe_2O_3 and Fe_2O_3@N-C.

Table 3
Summary of the EIS fitted parameters, ion conductivity and Warburg factor of the samples

Samples	Fitted parameters			
	$R_e/(\Omega)$	$R_1/(\Omega)$	$\sigma/(\Omega\ s^{-1/2})$	$D/(cm^2s^{-1})$
Fe_2O_3	5.66	126.8	443.397	6.21×10^{-12}
Fe_2O_3@N-C	5.24	57.02	54.335	7.81×10^{-11}

Calculations indicate that the ionic conductivities of Fe_2O_3 and Fe_2O_3@N-C as electrode materials are 6.21×10^{-12} and 7.81×10^{-11} cm²/s, respectively. Furthermore, galvanostatic intermittent titration technique (GITT) analysis was employed to determine lithium-ion diffusion coefficients (D_{Li+}), with values ranging from 10^{-12} to10^{-9} $cm^2\ s^{-1}$ (Fig. S3). Fe_2O_3@N-C exhibits lower resistance and higher ionic conductivity, resulting in better electrochemical performance as an electrode material, consistent with Fig. 5.

To investigate morphological stability, cross-sectional SEM characterization was performed on Fe_2O_3-Co@NPC electrodes before and after cycling (Fig. 8). Figure 8a-b show pre-cycling SEM images, with measured thicknesses of 30 μm for the Cu foil (Fig. 8a) and 20.61 μm for the initial coating layer (Fig. 8b). Post-cycling images (Figs. 8c-d) demonstrate increased coating thickness (35.4 μm, Fig. 8c), attributable to Fe_2O_3 pulverization during cycling, resulting in 170% volumetric expansion - significantly lower than pure Fe_2O_3 (> 200%). This confirms that in situ ZIF-67 growth effectively mitigates Fe_2O_3 volume changes during cycling. Figure 8d reveals cycling-induced defects from heterogeneous volume changes, causing localized stress concentrations and material delamination[4].

As described above, the Fe_2O_3@N-C composite electrode demonstrates outstanding electrochemical performance. The enhancement in performance is primarily due to the following factors: (1) The original ZIF-67 structure retains abundant active centers and rich pores, ensuring rapid ion transport; (2) Fe_2O_3 encapsulated within the interlocking MOF pores provides buffering for stress-strain during the lithiation/delithiation process, contributing to durability of the electrode during prolonged cycling; (3) The synergistic interplay between the durable MOF framework and the encapsulated Fe_2O_3 significantly enhances the electrochemical performance of the material.

4. Conclusion

This research successfully produced Fe_2O_3 material through a simple chemical precipitation process, employing iron concentrate leachate as the source of iron, and Fe_2O_3@N-C material was fabricated by in-situ growth of ZIF-67 followed by carbonization. To solve the electrochemical problems related to

transition metal anodes, it was employed as lithium-ion battery anode material. The composite structure exhibits outstanding cycling durability and rate efficiency. After 300 cycles with the current density of 1A g^{-1}, the capacity achieved was up to 782.9 mAh g^{-1}. Even at a high current density of 5A g^{-1}, Fe_2O_3@N-C sustained a discharge capacity of 202.39 mAh g^{-1}. The enhanced electrochemical performance is due to the adaptable core-shell, which efficiently mitigates the volume expansion resulting from lithium deintercalation during cycling tests. The N carbon shell significantly improves electron transport efficiency. The outcomes of this research support the enhanced development of using iron concentrate as an Fe source in electrode material production.

Declarations

CRediT authorship contribution statement

Yihao Peng: Conceptualization; Data curation; Investigation. Yu Song: Data curation; Resources. Li Wang：Data curation. Yunke Wang: Data curation. Yin Li: Conceptualization; Data curation; Funding acquisition; Investigation. Yaochun Yao: Funding acquisition; Resources.

Declaration of competing interest

The authors declare that they have no known competing financial interests or personal relationships that could have appeared to influence the work reported in this paper.

Acknowledgements

This work is financial supported by National Natural Science Foundation of China (Grant No. 52567025), Yunnan Fundamental Research Projects (Grant NO. 202301BE070001-065, 202301AU070055), Scientific Research Fund Project of Yunnan Provincial Department of Education(2024J0750).

References

1. Nitta N, Wu F, Lee JT, Yushin G (2015) Li-ion battery materials: present and future. Mater Today 18:252–264
2. Chen Y, Kang Y, Zhao Y, Wang L, Liu J, Li Y, Liang Z, He X, Li X, Tavajohi N, Li B (2021) A review of lithium-ion battery safety concerns: The issues, strategies, and testing standards. J Energy Chem 59:83–99
3. Hossain MH, Chowdhury MA, Hossain N, Islam MA, Mobarak MH (2023) Advances of lithium-ion batteries anode materials—A review. Chem Eng J Adv 16:100569
4. Lou D, Chen S, Langrud S, Razzaq AA, Mao M, Younes H, Xing W, Lin T, Hong H (2022) Scalable Fabrication of Si-Graphene Composite as Anode for Li-ion Batteries. Appl Sci 12(21):10926

5. Fang S, Bresser D, Passerini S (2022) Transition Metal Oxide Anodes for Electrochemical Energy Storage in Lithium- and Sodium-Ion Batteries. Adv Energy Mater Adv Energy Mater, : 55–99
6. Chen C, Duan F, Zhao S, Wang W, Yang F, Nuansing W, Zhang B, Qin Y, Knez M (2019) Porous Fe_2O_3 nanotubes with α-γ phase junction for enhanced charge separation and photocatalytic property produced by molecular layer deposition. Appl Catal B 248:218–225
7. Yao J, Yang Y, Li Y, Jiang J, Xiao S, Yang J (2021) Interconnected α-Fe2O3 nanoparticles prepared from leaching liquor of tin ore tailings as anode materials for lithium-ion batteries. J Alloys Compd, 855
8. Chen Z, Zhang C, Hua Y, Bie J, Chen B, Liang X, Liu G (2024) High-capacity and long-life Fe_2O_3/MOFs composite anodes: Preparation, characterization, morphology regulation and electrochemical performance. J Energy Storage 100:113512
9. Roy P, Srivastava SK (2015) Nanostructured anode materials for lithium ion batteries. J Mater Chem A 3:2454–2484
10. Cho JS, Park J-S, Kang YC (2016) Preparation of hollow Fe_2O_3 nanorods and nanospheres by nanoscale kirkendall diffusion, and their electrochemical properties for use in lithium-ion batteries. Sci Rep 6:38933
11. Benhammada A, Trache D, Kesraoui M, Tarchoun AF, Chelouche S, Mezroua A (2020) Synthesis and characterization of α-Fe_2O_3 nanoparticles from different precursors and their catalytic effect on the thermal decomposition of nitrocellulose. Thermochimica acta 686:178570
12. Zhang R, Sun M, Zhao G, Yin G, Liu B (2019) Hierarchical Fe_2O_3 nanorods/TiO2 nanosheets heterostructure: Growth mechanism, enhanced visible-light photocatalytic and photoelectrochemical performances. Appl Surf Sci 475:380–388
13. Sun M, Sun M, Yang H, Song W, Nie Y, Sun S (2017) Porous Fe_2O_3 nanotubes as advanced anode for high performance lithium ion batteries. Ceram Int 43:363–367
14. Wang H, Sun W, Liang X, Zou H, Jiao X, Lin KA, Li T (2021) Two-dimensional Fe_2O_3 nanosheets as adsorbent for the removal of Pb(II) from aqueous solution. J Mol Liq 335:116197
15. Han H, Riboni F, Karlicky F, Kment S, Goswami A, Sudhagar P, Yoo J, Wang L, Tomanec O, Petr M, Haderka O, Terashima C, Fujishima A, Schmuki P (2017) Zboril, α-Fe_2O_3/TiO_2 3D hierarchical nanostructures for enhanced photoelectrochemical water splitting†. Nanoscale 91:134–142
16. Jin Y, Dang L, Zhang H, Song C, Lu Q, Gao F (2017) Synthesis of unit-cell-thick α-Fe_2O_3 nanosheets and their transformation to γ-Fe_2O_3 nanosheets with enhanced LIB performances. Chem Eng J 326:292–297
17. Xu W, Yao J, Liu Z, Jiang J, Xiao S, Li Y (2025) Amorphous porous $FePO_4$/reduced graphene oxide nanocomposite cathode material prepared from the leaching solution of jarosite residue with excellent lithium/sodium storage performance. J Power Sources 632:236401
18. Zheng Y, Li Y, Huang R, Huang Y, Yao J, Huang B, Dubale AA (2019) Fabrication of 2D NiO Porous Nanosheets with Superior Lithium Storage Performance via a Facile Thermal-Decomposition

Method. ACS Appl Energy Mater 2:8262–8273

19. Safaei M, Foroughi MM, Ebrahimpoor N, Jahani S, Omidi A, Khatami M (2019) A review on metal-organic frameworks: Synthesis and applications. TRAC Trends Anal Chem 118:401–425
20. Zhang Y, Yu X, Hou Y, Liu C, Xie G, Chen X (2024) Current research status of MOF materials for catalysis applications. Mol Catal 555:113851
21. Jiao L, Seow JYR, Skinner WS, Wang ZU, Jiang H-L (2019) Metal–organic frameworks: Structures and functional applications, Materials Today, 27 43–68
22. Muthukumaran MK, Govindaraj M, Kogularasu S, Sriram B, Raja BK, Wang S-F, Chang-Chien G-P, Selvi A (2025) Recent advances in metal-organic frameworks for electrochemical sensing applications. Talanta Open 11:100396
23. Dutt S, Kumar A, Singh S (2023) Synthesis of Metal Organic Frameworks (MOFs) and Their Derived Materials for Energy Storage Applications. in: Clean Technologies, pp 140–166
24. Bhoite AA, Patil KV, Redekar RS, Jang JH, Sawant VA, Tarwal NL (2023) Recent advances in Metal-Organic Framework (MOF) derived metal oxides and their composites with carbon for energy storage applications. J Energy Storage 72:108557
25. Shi Y, Zhu B, Guo X, Li W, Ma W, Wu X, Pang H (2022) MOF-derived metal sulfides for electrochemical energy applications. Energy Storage Mater 51:840–872
26. Zhou W, Tang Y, Zhang X, Zhang S, Xue H, Pang H (2023) MOF derived metal oxide composites and their applications in energy storage. Coord Chem Rev 477:214949
27. Shahzadi S, Akhtar M, Arshad M, Ijaz MH, Janjua MRSA (2024) A review on synthesis of MOF-derived carbon composites: innovations in electrochemical, environmental and electrocatalytic technologies. RSC Adv 14:27575–27607
28. Huang S, Shi X-R, Sun C, Duan Z, Ma P, Xu S (2020) The Application of Metal–Organic Frameworks and Their Derivatives for Supercapacitors. Nanomaterials 10(11):2268
29. Cai D, Li D, Ding L-X, Wang S, Wang H (2016) Interconnected α-Fe_2O_3 nanosheet arrays as high-performance anode materials for lithium-ion batteries. Electrochim Acta 192:407–413
30. González-Banciella A, Martinez-Diaz D, de Prado J, Utrilla MV, Sánchez M, Ureña A (2024) MOF-derived α-Fe_2O_3@Fe_3O_4 on carbon fiber fabric for lithium-ion anode applications. J Energy Storage 90:111904
31. Kong L, Sun Y, Chu H, Xu S, Pan Z, Pan H, Zhao S, Li D (2024) Enhanced nonlinear optical response and ultrafast carrier dynamics in amorphous Fe-doped ZIF-67. Mater Chem Front 88:1971–1980
32. Zhang X, Wu H, Wang Y, Wang Y, Deng Y, Zhu Y, Zhang S, Rijnaarts H, Bruning H, Qin J, Lin Q, Ni Z, Qiu R (2025) Enhancing electrochemical reductive defluorination of PFASs using ZIF-67 modified cathode: Mechanistic insights and performance optimization. Water Res 268:122625
33. Wan X, Wu R, Deng J, Nie Y, Chen S, Ding W, Huang X, Wei Z (2018) A metal–organic framework derived 3D hierarchical Co/N-doped carbon nanotube/nanoparticle composite as an active electrocatalyst for oxygen reduction in alkaline electrolyte. J Mater Chem A 68:3386–3390

34. Wang M, Xi F, Li S, Ma W, Wan X, Tong Z, Luo B (2023) ZIF-67-derived porous nitrogen-doped carbon shell encapsulates photovoltaic silicon cutting waste as anode in high-performance lithium-ion batteries. J Electroanal Chem 931:117210
35. Jin D, Yang X, Ou Y, Rao M, Zhong Y, Zhou G, Ye D, Qiu Y, Wu Y, Li W (2020) Thermal pyrolysis of Si@ZIF-67 into Si@N-doped CNTs towards highly stable lithium storage. Sci Bull 656:452–459
36. Zhang K, Mao H, Gu X, Song C, Yang J, Qian Y (2020) ZIF-Derived Cobalt-Containing N-Doped Carbon-Coated SiO_x Nanoparticles for Superior Lithium Storage. ACS Appl Mater Interfaces 126:7206–7211
37. Cho JS, Hong YJ, Lee J-H, Kang YC (2015) Design and synthesis of micron-sized spherical aggregates composed of hollow Fe_2O_3 nanospheres for use in lithium-ion batteries. Nanoscale 718:8361–8367
38. Li Y, Huang Y, Zheng Y, Huang R, Yao J (2019) Facile and efficient synthesis of α-Fe_2O_3 nanocrystals by glucose-assisted thermal decomposition method and its application in lithium ion batteries. J Power Sources 416:62–71
39. Xu Y, Jian G, Liu Y, Zhu Y, Zachariah MR, Wang C (2014) Superior electrochemical performance and structure evolution of mesoporous Fe_2O_3 anodes for lithium-ion batteries. Nano Energy 3:26–35
40. Kim H, Choi W, Yoon J, Um JH, Lee W, Kim J, Cabana J, Yoon W-S (2020) Exploring Anomalous Charge Storage in Anode Materials for Next-Generation Li Rechargeable Batteries. Chem Rev 12014:6934–6976
41. Wang Q, Wang B, Zhang Z, Zhang Y, Peng J, Zhang Y, Wu H (2018) Tailoring yolk–shell FeP@carbon nanoboxes with engineered void space for pseudocapacitance-boosted lithium storage†. Inorg Chem Front 5(10):2605–2614
42. Li Y, Hui C, Hu J, Wang L, Yao Y (2024) Preparation of $FePO_4$ from leaching liquor of FeP waste slag and its application in lithium ions batteries. Solid State Ionics 412:116588
43. Zhao T, Zhu D, Li W, Li A, Zhang J (2019) Novel design and synthesis of carbon-coated porous silicon particles as high-performance lithium-ion battery anodes. J Power Sources 439:227027
44. Wang Y, Wu H, Huang L, Zhao H, Liu Z, Chen X, Liu H, Zhang Y (2018) Hierarchically Porous N,S-Codoped Carbon-Embedded Dual Phase MnO/MnS Nanoparticles for Efficient Lithium Ion Storage. Inorg Chem 5713:7993–8001

Scheme

Scheme 1 is available in the Supplementary Files section.

Figures

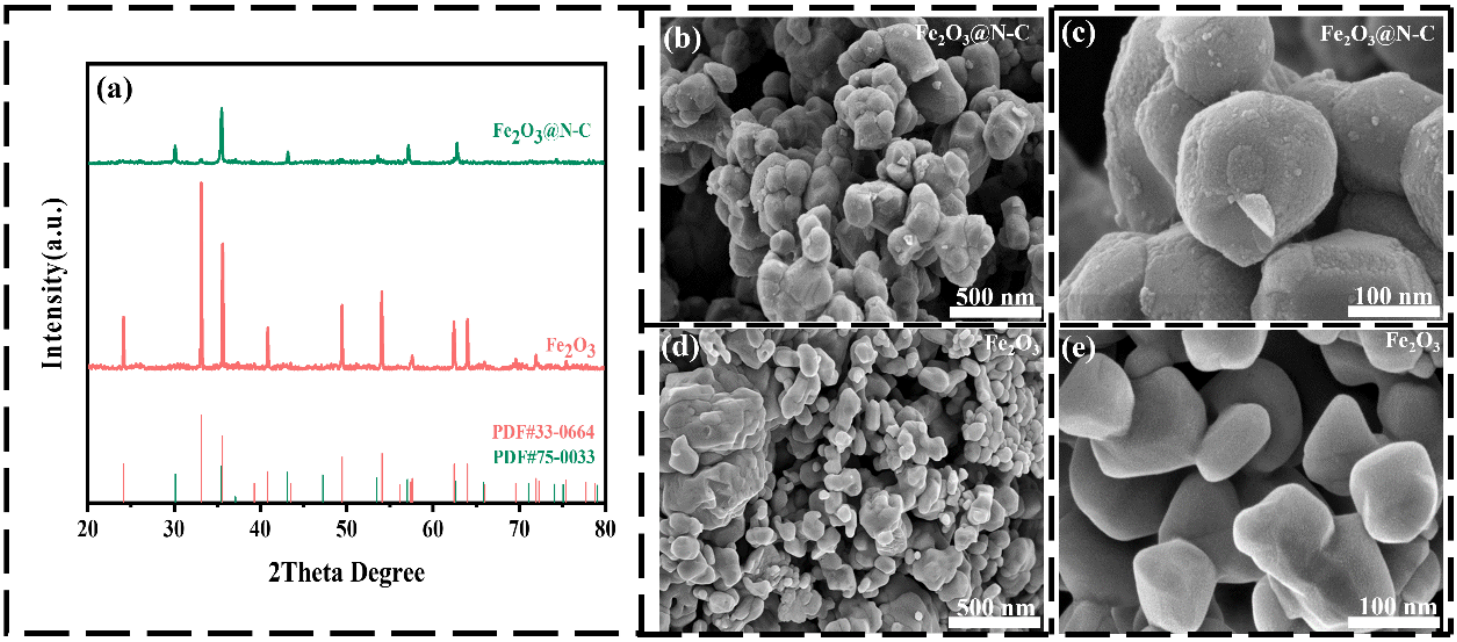


Figure 1

XRD spectra of Fe_2O_3 and Fe_2O_3@N-C (a); SEM images of Fe_2O_3 and Fe_2O_3@N-C (b-e).

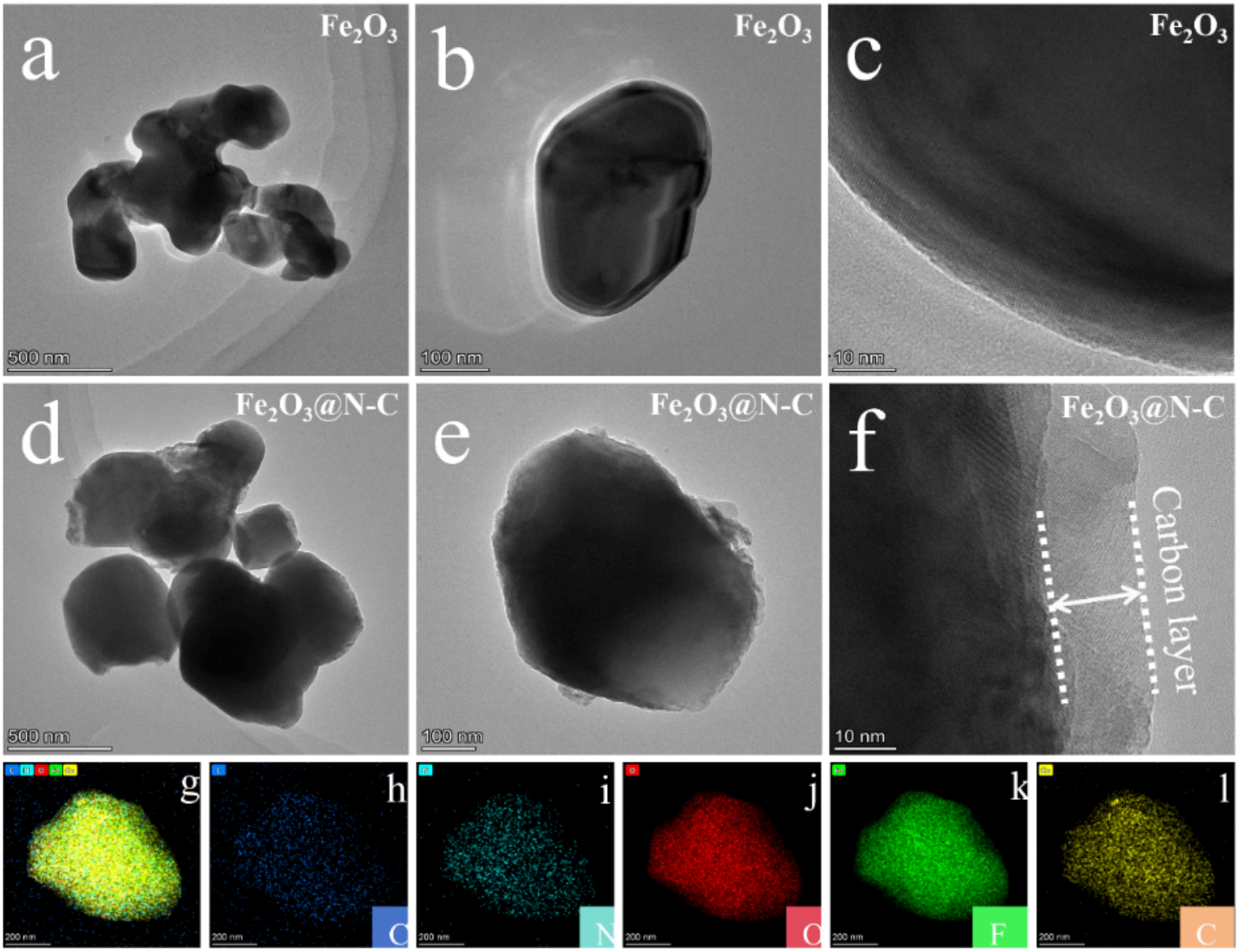


Figure 2

TEM images of Fe_2O_3 at various magnifications (a-c); TEM images of Fe_2O_3@N-C at various magnifications (d-f); Elemental mapping images of Fe_2O_3@N-C.

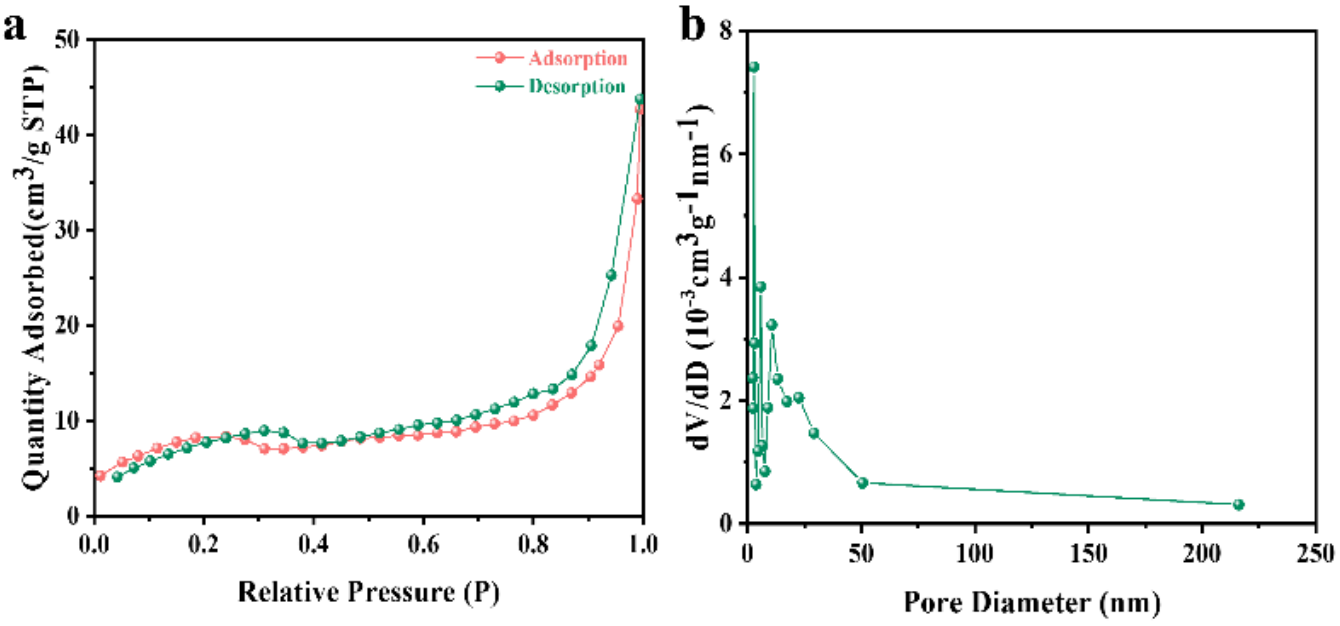


Figure 3

presents the N_2 adsorption/desorption isotherms (a); Alongside the pore size distribution charts (b) for Fe_2O_3@N-C.

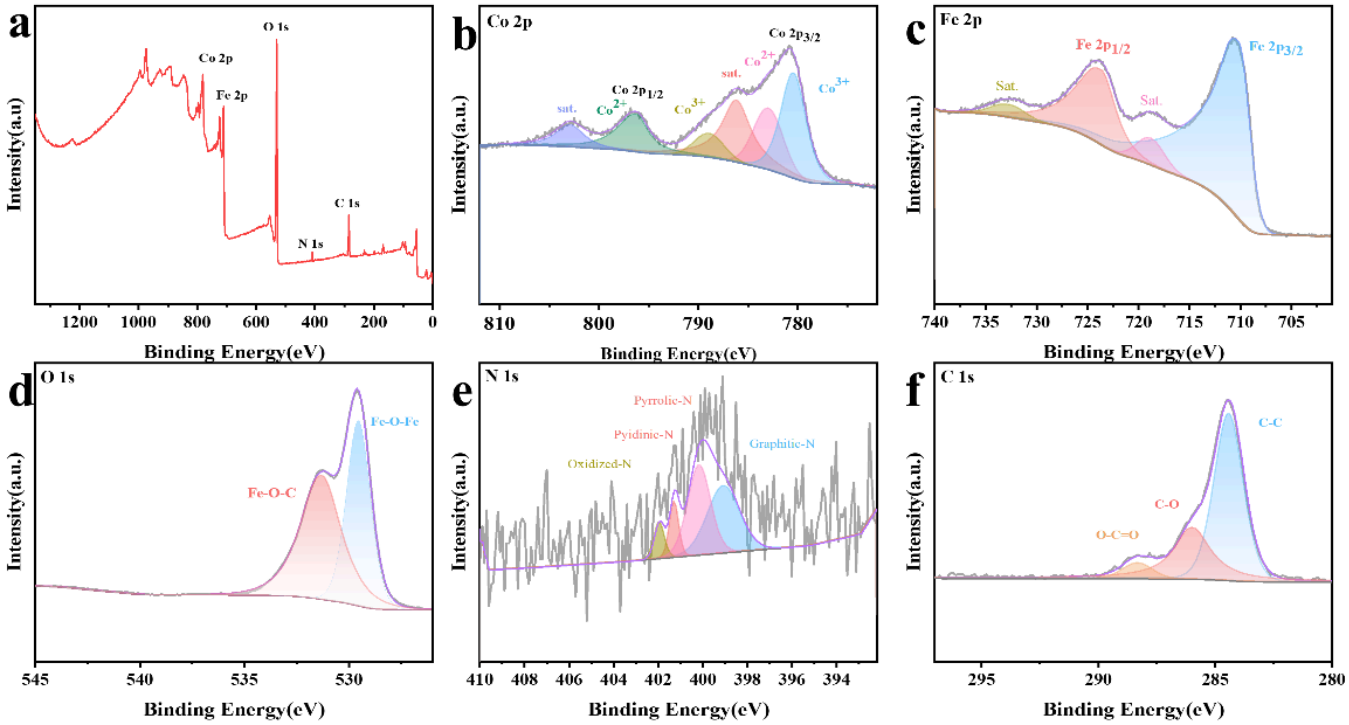


Figure 4

XPS spectra of Fe_2O_3@N-C: (a) complete survey spectrum, (b) Co 2p, (c) Fe 2p, (d) O 1s, (e) N 1s and (f) C 1s.

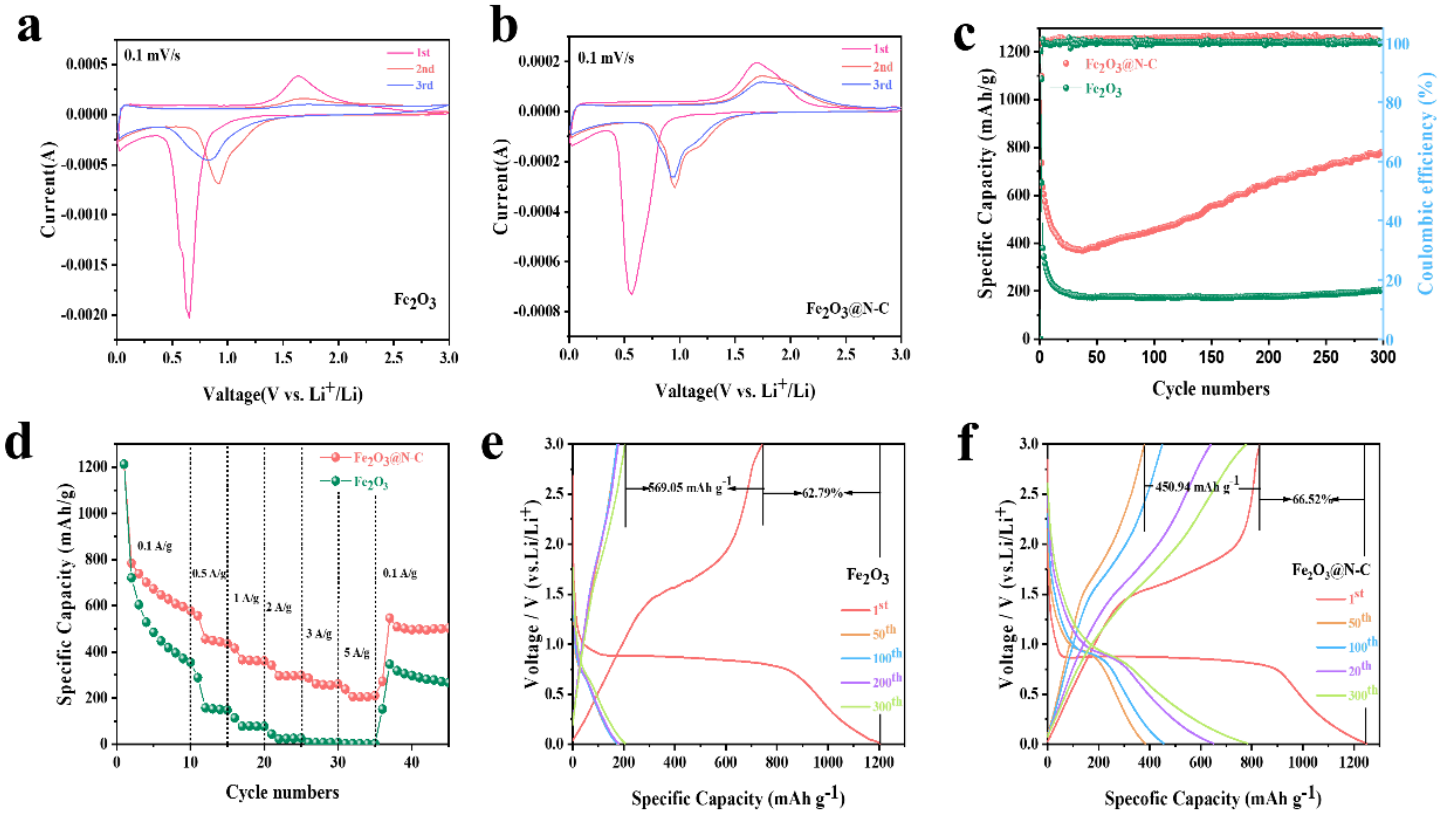


Figure 5

CV curves of Fe_2O_3 (a) and Fe_2O_3@N-C (b) in the initial, second, and third cycles at a rate of 0.1 mV/s; Long cycling performance at a current density of 1 A g^{-1} (c); Performance metrics at multiple current densities (d); Charge and discharge profiles of Fe_2O_3 (e) and Fe_2O_3@N-C (f) across various cycle counts.

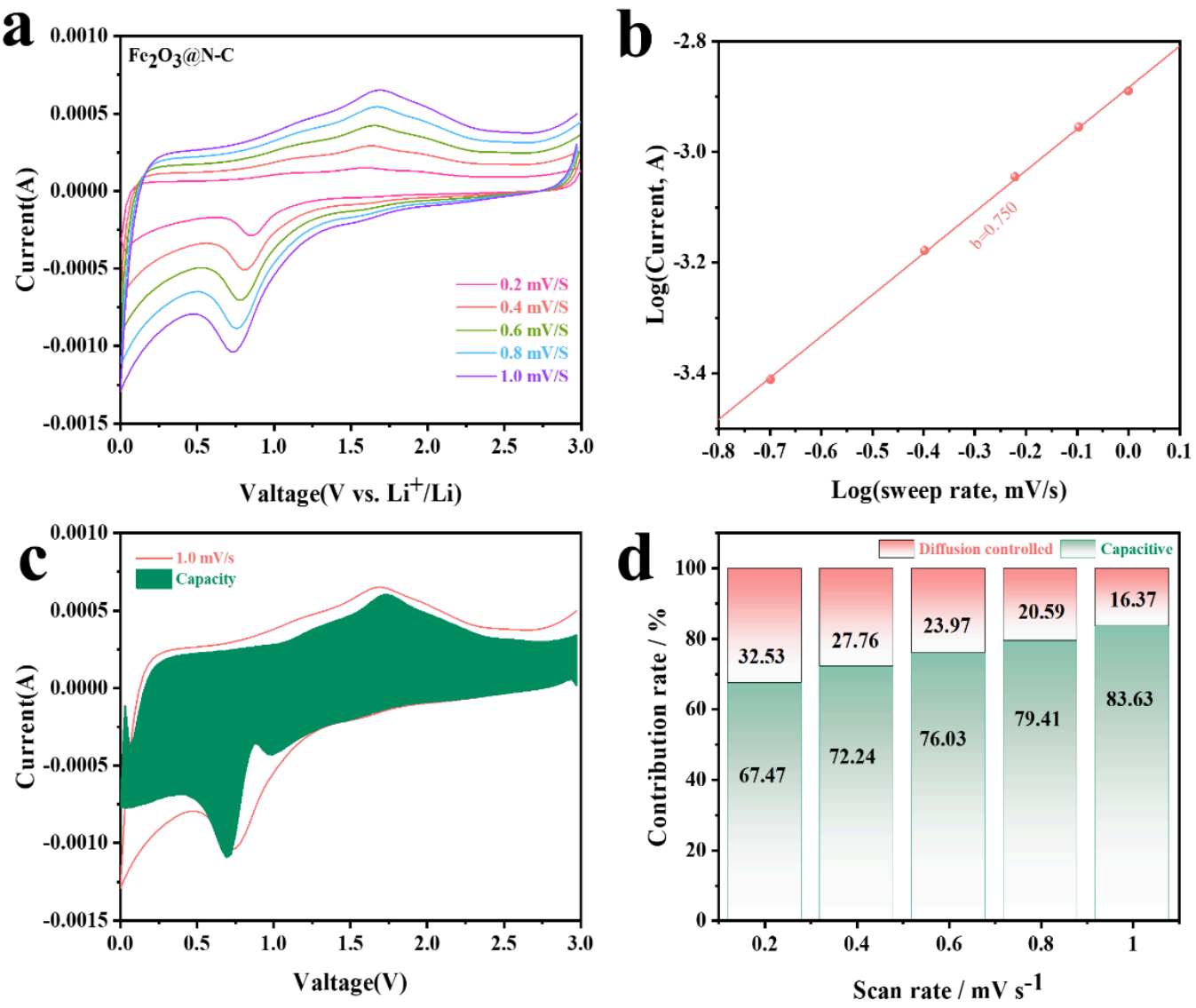


Figure 6

CV curves of Fe_2O_3@N-C at varying scan rates (a); Logarithms of peak current and scan rate are linearly related (b); Pseudocapacitance contribution percentage with a scanning speed of 1.0 mV s^{-1} (c); the pseudocapacitance and diffusion-controlled elements at several scanning rates for Fe_2O_3@N-C (d).

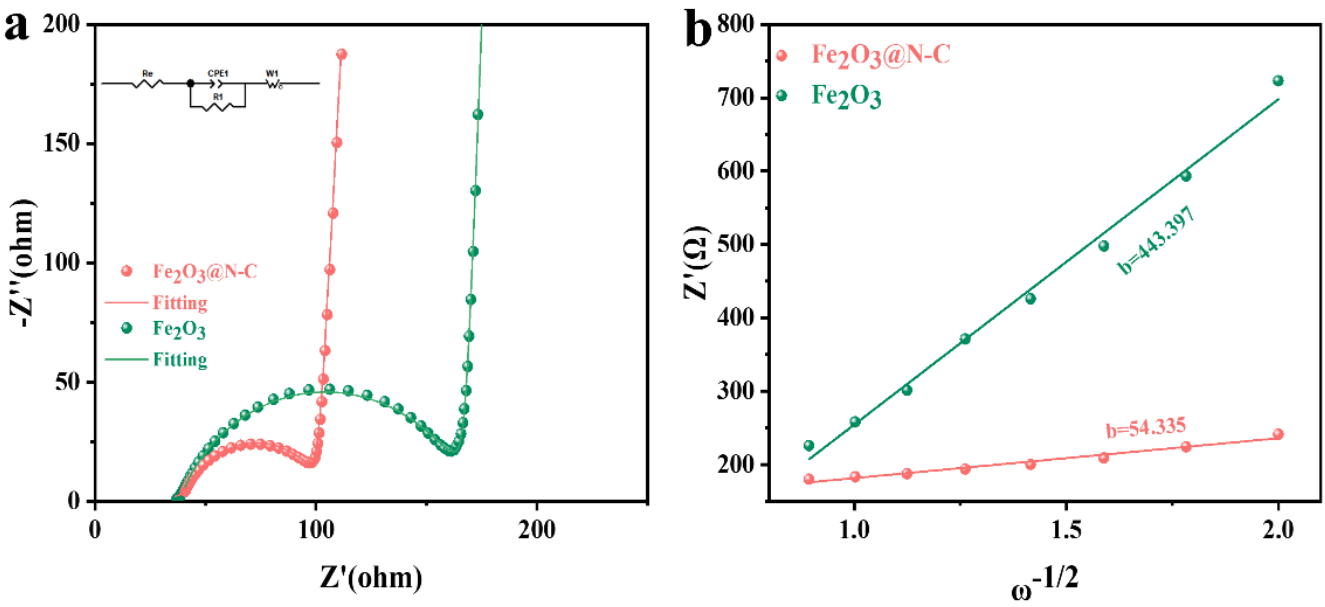


Figure 7

The Nyquist diagrams (a) and the straight-line correlation between Z' and $\omega^{-1/2}$ (b) for Fe_2O_3 and Fe_2O_3@N-C.

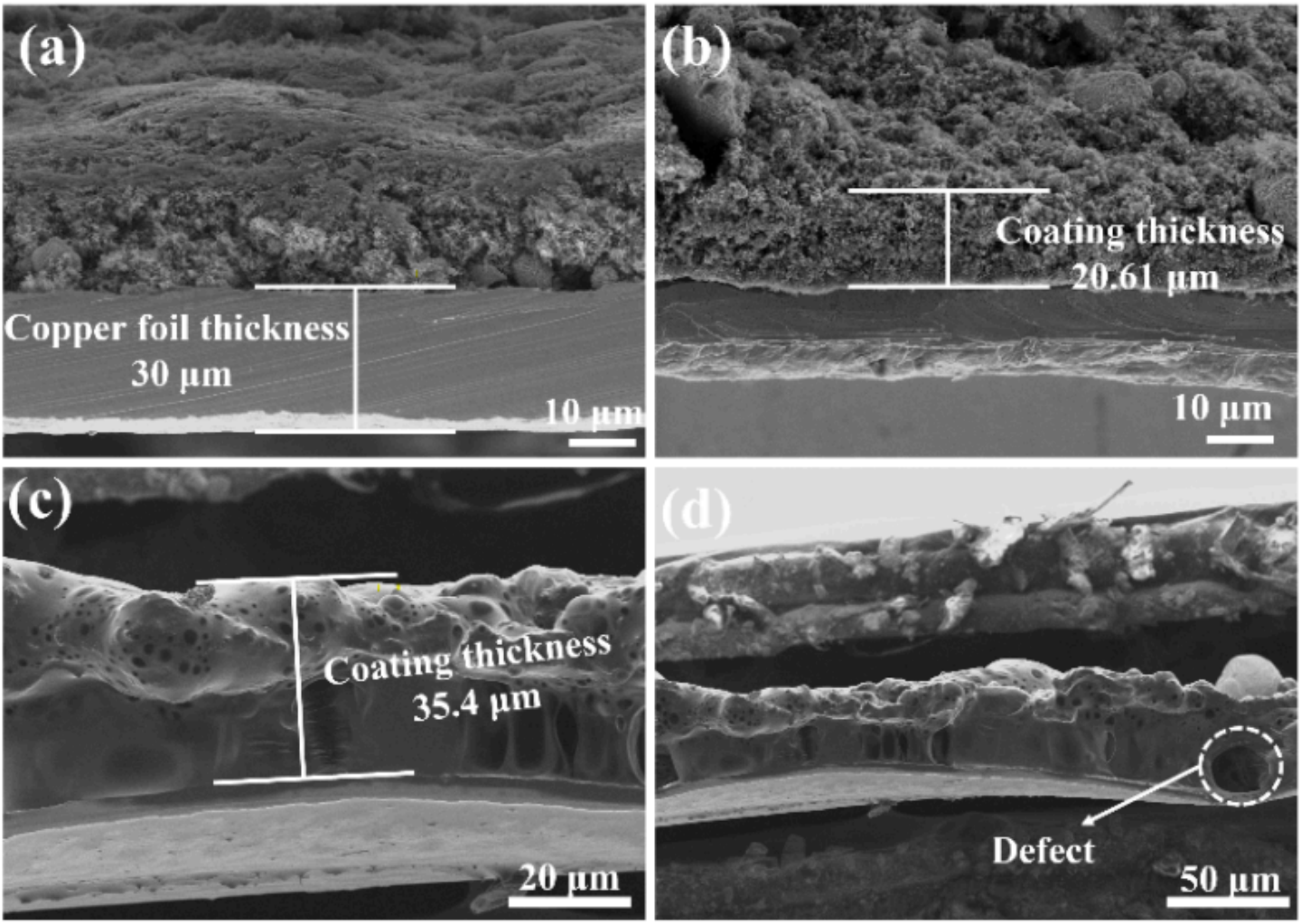


Figure 8

SEM images of Fe_2O_3@N-C electrodes before and after cycling (a,b); Pristine electrode morphology(c,d) After 300 cycles at 1A g^{-1}.

Supplementary Files

This is a list of supplementary files associated with this preprint. Click to download.

- SupplementaryInformation.docx
- Scheme.docx